Acta Pharmaceutica Sinica B 2025;15(1):424–437

Chinese Pharmaceutical Association
Institute of Materia Medica, Chinese Academy of Medical Sciences

Acta Pharmaceutica Sinica B

www.elsevier.com/locate/apsb
www.sciencedirect.com

ORIGINAL ARTICLE

Cyclometalated iridium(III) complex based on isoquinoline alkaloid synergistically elicits the ICD response and IDO inhibition *via* autophagy-dependent ferroptosis

Yuan Lu [a,b,†], Shan-Shan Wang [a,†], Meng-Ya Li [a,†], Rong Liu [a], Meng-Fan Zhu [a], Liang-Mei Yang [a], Feng-Yang Wang [a], Ke-Bin Huang [a,*], Hong Liang [a,*]

[a]*State Key Laboratory for Chemistry and Molecular Engineering of Medicinal Resources, Key Laboratory for Chemistry and Molecular Engineering of Medicinal Resources (Ministry of Education of China), Collaborative Innovation Center for Guangxi Ethnic Medicine, School of Chemistry and Pharmaceutical Sciences, Guangxi Normal University, Guilin 541004, China*
[b]*Department of Pharmacy, School of Medicine, Guangxi University of Science and Technology, Liuzhou 545005, China*

Received 26 May 2024; received in revised form 18 June 2024; accepted 19 June 2024

KEY WORDS

Organometallic complex;
Cyclometalated iridium complex;
Isoquinoline alkaloid;
ER stress;
Autophagy-dependent ferroptosis;
Immunogenic cell death;
IDO inhibition;
Chemoimmunotherapy

Abstract The development of anticancer drugs to treat triple-negative breast cancer (TNBC) is an ongoing challenge. Immunogenic cell death (ICD) has garnered considerable interest worldwide as a promising synergistic modality for cancer chemoimmunotherapy. However, only few drugs or treatment modalities can trigger an ICD response and none of them exert a considerable clinical effect against TNBC. Therefore, new agents with potentially effective chemoimmunotherapeutic response are required. In this study, five new cyclometalated Ir(III) complexes containing isoquinoline alkaloid CN ligands were designed and synthesized. Among them, **Ir-1** exhibited the highest *in vitro* cytotoxicity. Mechanistically, **Ir-1** could trigger autophagy-dependent ferroptosis and a subsequent ferroptosis-dependent ICD response as well as indoleamine 2,3-dioxygenase (IDO) inhibition *via* reactive oxygen species (ROS)-mediated endoplasmic reticulum (ER) stress in MDA-MB-231 cells. When immunocompetent BALB/c mice were vaccinated with **Ir-1**-treated dying TNBC cells, antitumor $CD8^+$ T-cell response and $Foxp3^+$ T-cell depletion were induced, resulting in long-lasting antitumor immunity in TNBC cells. Moreover,

*Corresponding authors.
E-mail addresses: kbhuang@mailbox.gxnu.edu.cn (Ke-Bin Huang), hliang@gxnu.edu.cn (Hong Liang).
[†]These authors made equal contributions to this work.
Peer review under the responsibility of Chinese Pharmaceutical Association and Institute of Materia Medica, Chinese Academy of Medical Sciences.

https://doi.org/10.1016/j.apsb.2024.06.017

combination therapy with **Ir-1** and anti-PD1 could substantially augment *in vivo* therapeutic effects. Based on these results, **Ir-1** is a promising candidate for chemoimmunotherapy against TNBC and its effects are mediated synergistically *via* ICD induction and IDO blockage.

1. Introduction

Globally, breast cancer is the most prevalent cancer among women. It has the highest incidence among the commonly diagnosed cancers reported in GLOBOCAN 2020[1]. Although notable progress has been made in breast cancer treatment over recent decades, the survival rate of patients with triple-negative breast cancer (TNBC), accounting for 10%−30% of all breast cancers[2], is relatively low because of its high metastatic capacity and limited pharmacological treatment options. Presently, immunotherapy is revolutionizing the treatment of TNBC, for example, the early administration of immune-checkpoint inhibitors (ICIs) during the disease course of TNBC has proven therapeutically efficacious[3,4]. Moreover, the use of ICIs alongside chemotherapy can considerably improve the overall survival of patients with TNBC[5,6].

Accumulating clinical studies have reported that conventional chemotherapeutic drugs not only induce direct cell inhibition/cytotoxicity against fast-growing cancer cells but also reactivate tumor-specific immune responses[7,8]. One of the several ways by which chemotherapeutic drugs activate tumor-specific immune responses is by inducing immunogenic cell death (ICD), wherein dying cancer cells function as "anticancer vaccines", eliciting a strong adaptive immune response[9,10]. To date, several clinical chemotherapeutic agents have exhibited promising ICD activity, including doxorubicin, cyclophosphamide, and oxaliplatin (Oxa)[11,12]. However, the current ICD-inducing drugs are insufficient because the induction of ICD can depend on tumor types. For example, Oxa cannot trigger ICD in non-small cell lung cancer[13]. Therefore, novel anticancer complexes that can be employed as more efficient ICD inducers are urgently required. In addition to Oxa, some metal complexes based on Pt[14-26], Ru[27-30], Ir[31-39], Cu[40], Au[41-47], Mn[48], and Re[49] reportedly promote the ICD effect against tumor cells. For example, Sen and coworkers reported a rationally designed redox-active metal complex, Au(I) N-heterocyclic carbene (NHC), that could induce ICD[42]. Our group designed a Pt(II) complex containing an aminophosphonate ester ligand that selectively accumulated in the endoplasmic reticulum (ER) and triggered type II ICD[14]. Additionally, although the concept of ICD was initially proposed in chemotherapy-induced apoptosis, ICD can also be triggered in the other modes of programmed cell deaths caused by radiotherapy, chemotherapy, photodynamic therapy, or other anticancer treatments[50].

Organometallic complexes have unique properties, including structural diversity, ligand exchange, redox and catalytic properties, making them promising drug candidates for cancer therapy[51]. Cyclometalated complexes are specific types of organometallic complexes that exhibit attractive biological properties. The anticancer effects of these complexes can primarily be ascribed to the C^N ligands that form the cyclometalated backbone[52,53]. Under physiological conditions, the chelating feature of the C^N ligand and the robust metal−carbon bond in these complexes ensure structural integrity, thereby enabling the targeting of the cancer cells without ligand detachment[54]. Recently, several cyclometalated complexes were reported to possess ICD-inducing capacity. For example, Tham et al. identified two cyclometalated Pt(II)-based NHC complexes as a new category of type II ICD inducers[19]. Among non-platinum cyclometalated compounds, iridium complexes have attracted considerable attention as ICD inducers. Wang et al. reported a cyclometalated Ir(III) complex containing an *N*,*N*-bis(2-chloroethyl)-azane derivate that targeted the ER and acted as a type II ICD inducer in human non-small cell lung cancer cells[31], and another cyclometalated Ir(III) complex containing 2-phenylbenzo[d]-thiazole ligand as a promising ICD-inducing photosensitive agent in melanoma cells for two-photon photodynamic immunotherapy[36]. Vigueras et al. developed a cyclometalated Ir(III) complex based on benzimidazole that induced a type II ICD effect against melanoma upon blue-light irradiation[33]. Tan and Mao's group developed ferrocene-containing cyclometalated Ir(III) complexes that induced ICD in cancer cells[34,35] and a phenylquinoline-containing cyclometalated Ir(III) photosensitizer that induced ICD under hypoxia[37]. In addition, our group reported a cyclometalated Ir(III)−bisNHC complex as a novel ICD inducer[38]. Overall, cyclometalated Ir(III) complexes are potential candidates for developing more effective ICD inducers against TNBC tumors.

To develop more active metal-based therapeutic agents with lower side effects, natural active products or their derivatives used as ligands can produce novel metal-based agents[55,56]. Previously, our group reported a series of metal complexes bearing natural active (iso)quinoline alkaloids or their derivative ligands as promising anticancer candidates[57,58]. As our continuing research, we focused on the isoquinoline alkaloid derivative used as the C^N structure of cyclometalated Ir(III) complexes, which may change the lipophilicity and electronic properties of the complexes, thereby enhancing their druggability. Herein, a series of cationic cyclometalated Ir(III) complexes including an isoquinoline alkaloid derivative known as cyclometalated C^N ligand and different bidentate N^N ancillary ligands were designed, synthesized, and characterized. The cationic cyclometalated Ir(III) complexes exhibited higher potency against TNBC cell lines than cisplatin. This study demonstrates that our complex has the following advantages: 1) novel approach for TNBC chemoimmunotherapy *via* a new cyclometalated Ir(III) complex using isoquinoline alkaloid as a C^N ligand, 2) a new regulatory mechanism of ICD mediated by autophagy-dependent ferroptosis, and 3) a synergistically elicited chemoimmunotherapy response achieved by combining ICD and indoleamine 2,3-dioxygenase (IDO) inhibition. This study is expected to create new avenues for the development of novel iridium-based chemoimmunotherapy agents against TNBC.

2. Results and discussion

2.1. Synthesis and characterization

To develop metal-based scaffolds with novel anticancer mechanisms, cyclometalated Ir(III) complexes (**Ir-1**−**Ir-5**) were designed bearing two identical CN isoquinoline derivative ligands and structurally diverse N^N ligands (Scheme 1). For the isoquinoline ligand 3,4-methylenedioxy-1-phenylisoquinoline (L_a)[59], a phenyl group was introduced at the 1-position of the isoquinoline ring to facilitate the formation of the CN structure with iridium as the metal center. Furthermore, methoxy cyclopentane, a commonly used pharmacophore group, was designed to regulate the lipophilicity and bioactivity of the Ir(III) complexes. For the structurally diverse N^N ligands, **Ir-1** carries a substituted 2,2-dipyridinine amine scaffold (L_1), **Ir-2** carries the 1,10-phenanthroline N^N ligand (L_2), **Ir-3** bears the 2-(2-pyridyl) benzimidazole ligand (L_3), **Ir-4** contains the unsubstituted 2,2-bipyridine ligand (L_4), and **Ir-5** contains the 2-aminomethylpyridine ligand (L_5). To the best of our knowledge, this study is the first to report these five complexes. The synthetic routes for these iridium(III) complexes are depicted in Scheme 1. All new complexes were characterized by $^1H/^{13}C$ nuclear magnetic resonance (NMR) and electrospray ionization mass spectrometry (ESI-MS; see Supporting Information Experimental section and Figs. S1−S3). In subsequent studies, **Ir-1** presented superior biological activity; hence, **Ir-1** was further characterized *via* single crystal X-ray diffraction analysis (Fig. 1 and Supporting Information Table S1). The Ir(III) center is coordinated by a distorted octahedral geometry with two carbon atoms from L_a and two nitrogen atoms from auxiliary ligands L_1 in a cis orientation, which forms the equatorial coordination plane, while the axial positions are occupied by nitrogen atoms from two isoquinoline ligands L_a. The stability of complexes **Ir-1**−**Ir-5** at room temperature was confirmed *via* HPLC analysis in TBS. The HPLC

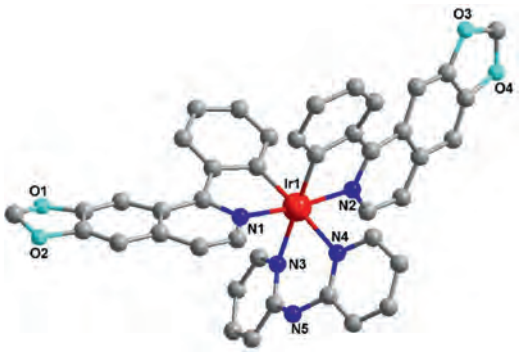

Figure 1 X-ray crystal structure of **Ir-1**. All hydrogen atoms have been removed for clarity. CCDC number: 2289402.

chromatograms at different times reveal no observable changes during the 24- and 48-h time courses, indicating that these cyclometalated Ir(III) complexes were stable in TBS for the tested time course (Supporting Information Fig. S4). Unless otherwise specified, the metal complexes were dissolved in dimethylformamide (DMF) to prepare a 2 mmol/L stock solution, and then diluted into aqueous solution for subsequent experiments.

2.2. In vitro cytotoxic activity

To investigate the *in vitro* anticancer activity of these cyclometalated Ir(III) complexes, the cytotoxicity of **Ir-1**−**Ir-5** and the isoquinoline ligand (L_a) was assessed against non-small cell lung carcinoma (NCl−H460, A549), human TNBC (MDA-MB-231), and human gastric adenocarcinoma (MGC-803) cells *via* 3-(4,5-dimethylthiazol-2-yl)-2,5-diphenyltetrazolium bromide (MTT) assays. Cisplatin was employed as a positive control. After 48 h of treatment with each compound, the IC_{50} values were derived (Table 1). The isoquinoline alkaloid ligand L_a did not show

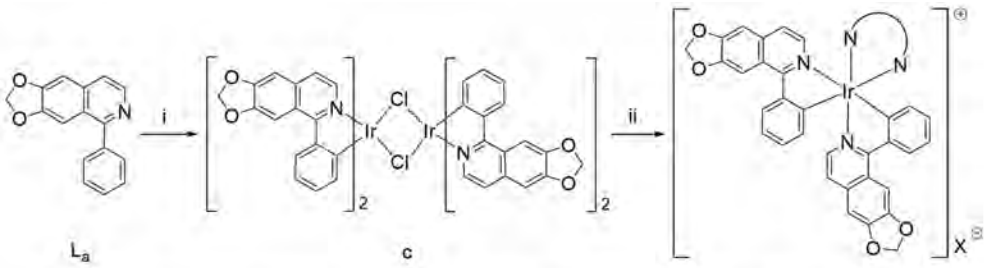

Complex	N^N	X	Complex	N^N	X
Ir-1	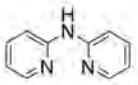	PF_6	Ir-2	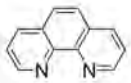	PF_6
Ir-3	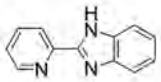	PF_6	Ir-4	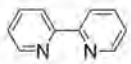	PF_6
Ir-5	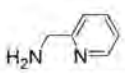	Cl			

Scheme 1 Synthetic route and structures of **Ir-1**−**Ir-5**. Reagent and conditions: (i) $IrCl_3 \cdot 3H_2O$, 2-ME/H_2O, N_2, 1 h, 120 °C; (ii) N^N ligand, $(CH_2OH)_2$, N_2, 2 h, 120 °C, and then KPF_6, for the synthesis of **Ir-1**−**Ir-4**; N^N ligand, CH_3OH, Na_2CO_3, N_2, 65 °C, 30 min, for the synthesis of **Ir-5**.

considerable cytotoxicity (IC_{50} > 20 μmol/L) against the tested cancer cell lines; however, all Ir(III) complexes (**Ir-1**−**Ir-5**) exhibited excellent cytotoxicity (IC_{50} = 1.73−8.62 μmol/L), indicating a synergistic effect derived from the coordination between the Ir(III) ion and ligands. Additionally, **Ir-1**−**Ir-5** demonstrated considerably higher cytotoxic activity than cisplatin (IC_{50} = 12.23−18.54 μmol/L) against the tested cell lines. Notably, **Ir-1** and **Ir-2** showed higher cytotoxic activity than the other three complexes, indicating that auxiliary ligands also play a substantial role in regulating the cytotoxicity of these iridium complexes bearing the isoquinoline alkaloid CN ligand. The differences in cytotoxicity among **Ir-1**−**Ir-5** may be attributed to the varying lipophilicity or electronic effects of their N^N ligands. Furthermore, **Ir-1**−**Ir-5** exhibited more sensitive cytotoxicity against the MDA-MB-231 cells than that against the other tested cell lines overall. Consequently, the MDA-MB-231 cell line was selected as the representative cancer cell line for further investigation of anticancer mechanism.

2.3. *Induction of ICD activity by **Ir-1***

As **Ir-1**−**Ir-5** exhibited excellent *in vitro* cytotoxicity against MDA-MB-231 cells and cyclometalated Ir(III) complexes had demonstrated ICD characteristics, we subsequently sought to discover whether the newly synthesized cyclometalated complexes could induce ICD in MDA-MB-231 cells. A key endogenous signal that induces the immunogenicity of tumor cells is the extracellular secretion of high mobility group protein 1 (HMGB1) from the nucleus[60]. We investigated the levels of HMGB1 in MDA-MB-231 cell supernatants after treating the cells with **Ir-1**−**Ir-5** (4 μmol/L). **Ir-1** and **Ir-2** could significantly induce the release of HMGB1 from MDA-MB-231 cells (Fig. 2A), although **Ir-1** induced a higher level of HMGB1 release than **Ir-2**. Notably, after **Ir-1** treatment, the extracellular level of HMGB1 showed a concentration-dependent increase (Fig. 2B), consistent with the concentration-dependent decreasing trend of intracellular HMGB1 levels (Fig. 2D). Overall, these results provide support for the suggestion that **Ir-1** may be a potential ICD inducer. The **Ir-1**-induced ICD activity and related mechanisms were subsequently investigated in MDA-MB-231 cells.

Another dominant damage-associated molecular pattern (DAMP) signal of ICD is the exposure of calreticulin (CRT) on the outer cell surface[60]. To assess the **Ir-1**-induced ICD activity, MDA-MB-231 cells were incubated with this complex and labeled with an anti-CRT antibody. Consequently, the immunofluorescence of CRT (green) was enhanced on the cell membrane surface (red) in a concentration-dependent manner (Fig. 2C), which indicated that potent CRT exposure had been induced in **Ir-1**-treated MDA-MB-231 cells. As anticipated, the secretion of ATP, another DAMP signal of ICD, was also observed in a concentration-dependent manner up to 215 nmol/L, after treatment with 4 μmol/L **Ir-1** (Fig. 2E). Overall, these results imply that **Ir-1** is a potential candidate of ICD inducer, which encouraged us to investigate related mechanisms underlying the induction of ICD activity by **Ir-1** in MDA-MB-231 cells.

2.4. *Reactive oxygen species (ROS) production and ER stress response induced by **Ir-1***

ER stress is essential for initiating ICD[9,10,61]. In addition to factors including nutrient deficiency, infection, and hypoxia, ROS generation can contribute to ER stress[62]. Several cyclometalated Ir(III) complexes have also been implicated in the induction of considerable ROS production and ER stress response[31,63-65]. Consequently, we investigated whether **Ir-1** could similarly cause ROS production and trigger an ER stress response. Initially, we sought to assess the ROS generation in **Ir-1**-induced MDA-MB-231 cells using a commercial ROS fluorescent indicator DCFH-DA[66]. Confocal micrographs revealed a time-dependent increase in ROS levels (Fig. 3A), suggesting that ROS might stimulate an ER stress response. Subsequently, we investigated whether **Ir-1** could induce ER stress. Alterations in expression levels of three ER-stress-related marker proteins, namely phosphorylated protein kinase RNA-like ER kinase (p-PERK), phosphorylated eukaryotic initiation factor 2α (p-eIF2α), and C/EBP homologous protein (CHOP), were determined in **Ir-1**-treated MDA-MB-231 cells. The expression levels of p-eIF2α, p-PERK, and CHOP were elevated (Fig. 3B), which are typical signs of ER stress. To delve deeper into whether an ER stress response was induced by ROS generation, an ROS scavenger, *N*-acetyl-L-cysteine (NAC), was co-incubated, and Western blotting of ER-stress-related proteins was conducted. The results revealed that alterations in the expression levels of p-eIF2α, p-PERK, and CHOP triggered by **Ir-1** were inhibited after pretreating the MDA-MB-231 cells with NAC (Fig. 3C). This suggests that the ER stress induced by **Ir-1** is dependent on ROS production. To explore the effect of ROS generation on **Ir-1**-induced cytotoxicity in MDA-MB-231 cells, we conducted an MTT assay using NAC as an ROS scavenger. There was a dose-dependent increase in cell viability, which increased from ∼48% (**Ir-1**-treated group) to ∼90% (10 mmol/L NAC- and **Ir-1**-treated group; Fig. 3D). This implies that ROS production considerably contributes to the induction of cell death. Collectively, these findings suggest that **Ir-1** triggers cell death through an ROS-mediated mechanism, accompanied by the induction of an ER stress response.

Table 1 IC_{50} values (μmol/L) of Ir(III) complexes, cisplatin, and ligand L_a toward four human tumor cell lines.

Complex	NCl−H460	A549	MGC-803	MDA-MB-231
Ir-1	2.03 ± 0.15	2.40 ± 0.12	2.60 ± 0.14	1.82 ± 0.10
Ir-2	2.12 ± 0.11	2.75 ± 0.20	2.85 ± 0.17	1.73 ± 0.14
Ir-3	7.78 ± 0.18	8.45 ± 0.35	8.62 ± 0.26	7.14 ± 0.25
Ir-4	3.10 ± 0.12	4.20 ± 0.16	3.90 ± 0.16	2.50 ± 0.17
Ir-5	5.70 ± 0.10	6.27 ± 0.24	6.40 ± 0.33	3.13 ± 0.22
Cisplatin	18.29 ± 0.62	18.54 ± 0.68	12.33 ± 0.43	12.23 ± 0.46
L_a	>20	>20	>20	>20

Data are presented as mean ± SD (n = 3).

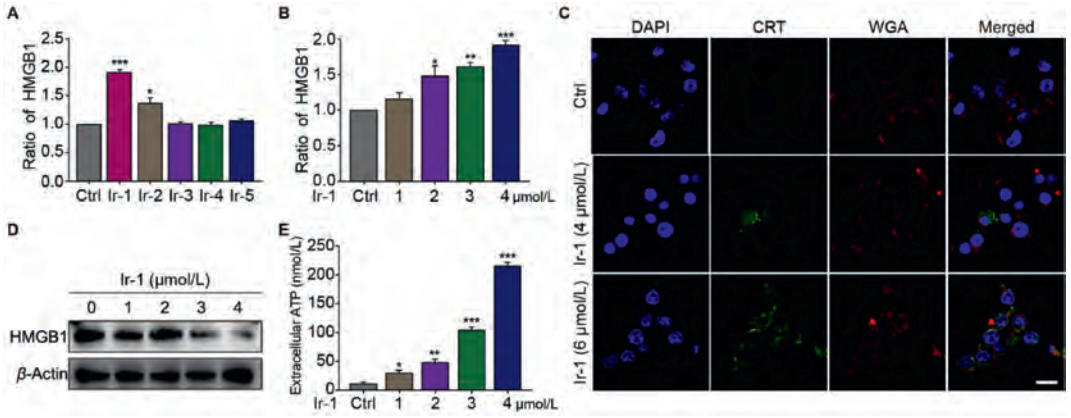

Figure 2 ICD activity induced by **Ir-1**. (A, B) Release of HMGB1 from MDA-MB-231 cells after treatment with (A) **Ir-1**−**Ir-5** (4 μmol/L) and (B) **Ir-1** (1−4 μmol/L) for 12 h, respectively. (C) Representative confocal images showing CRT exposure after treating MDA-MB-231 cells with **Ir-1** for 12 h. Scale bar = 20 μm. (D) Western blots of intracellular HMGB1 after treating MDA-MB-231 cells with **Ir-1** for 12 h. (E) Release of ATP from MDA-MB-231 cells after treatment with **Ir-1** for 12 h. Data are presented as mean ± SD ($n = 3$). $^{*}P < 0.05$, $^{**}P < 0.01$, $^{***}P < 0.001$, as compared with the control group.

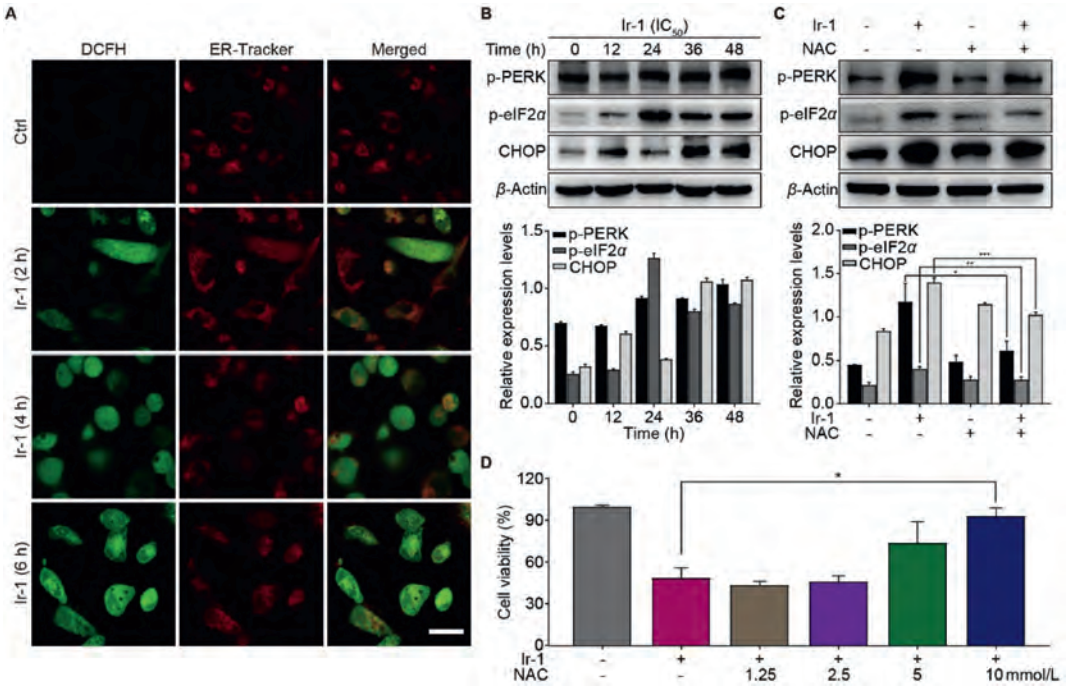

Figure 3 Induction of ROS production and ER stress by **Ir-1**. (A) Representative confocal micrographs of ROS production in MDA-MB-231 cells induced by **Ir-1** (at IC_{50}). Scale bar = 20 μm. (B) Western blots of ER-stress-related proteins after incubating MDA-MB-231 cells with **Ir-1**. (C) Western blots of ER-stress-related proteins after co-incubating MDA-MB-231 cells with NAC (10 mmol/L) and **Ir-1** (at IC_{50}) for 48 h. (D) Viability of MDA-MB-231 cells treated with NAC and **Ir-1** (at IC_{50}). Data are presented as mean ± SD ($n = 3$). $^{*}P < 0.05$, $^{**}P < 0.01$, $^{***}P < 0.001$, as compared with the indicated group.

2.5. *Modes of cell death triggered by **Ir-1***

ROS reportedly induces several types of cell death, including autophagy, ferroptosis, and apoptosis[67]. To determine the primary mode of cell death caused by the ROS effects induced by **Ir-1**, we employed several inhibitors targeting cell death-associated mechanisms to modulate the viability of cells treated with **Ir-1**. The commonly used apoptosis inhibitor Z-VAD-FMK did not significantly affect the viability of **Ir-1**-treated cells (Fig. 4A). 3-Methyladenine (3-MA) functions as an autophagy inhibitor[68]. After pretreating cells with 3-MA (0.5, 1, and 2 mmol/L), **Ir-1**-induced cell death was dose-dependently blocked (Fig. 4B). The viability of **Ir-1**-treated cells increased by ∼20% upon pretreatment with 2 mmol/L 3-MA, suggesting that the mode of cell death induced by **Ir-1** is related to autophagy. Furthermore, MDA-MB-231 cells pretreated with a ferroptosis inhibitor, ferrostatin-1

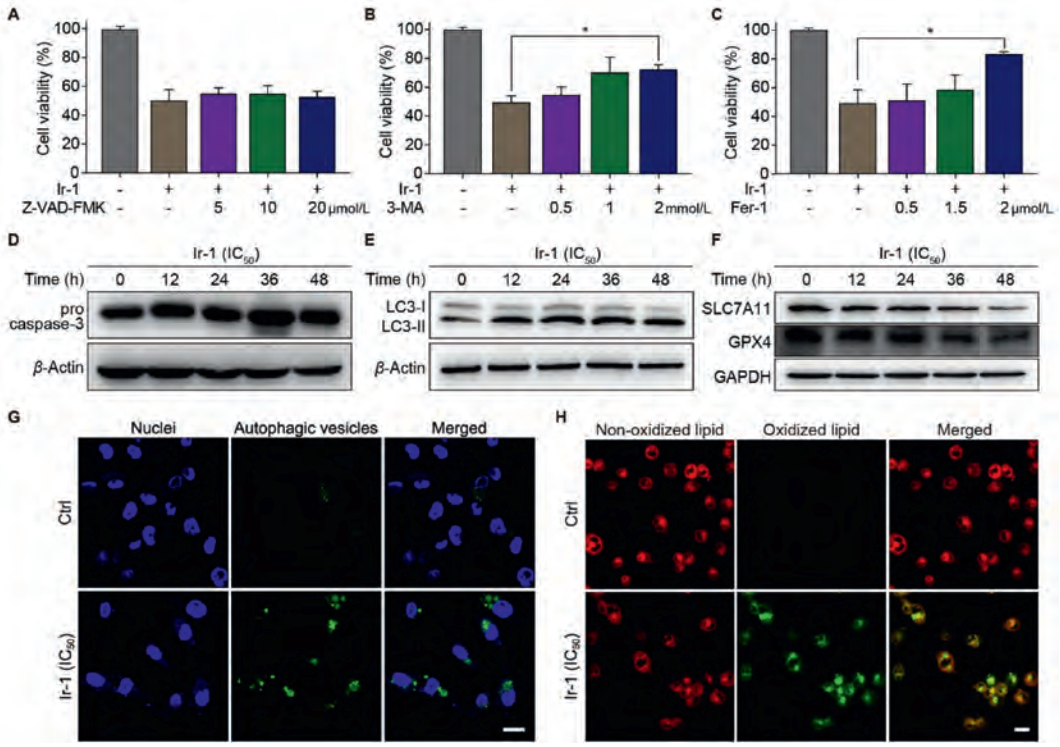

Figure 4 Induction of autophagy and ferroptosis by **Ir-1**. (A–C) Viability of MDA-MB-231 cells co-treated with (A) Z-VAD-FMK, (B) 3-MA, or (C) Fer-1, respectively, and **Ir-1** (at IC_{50}). (D–F) Western blots of (D) apoptosis, (E) autophagy, or (F) ferroptosis markers after incubating MDA-MB-231 cells with **Ir-1**. (G) Representative confocal micrographs showing autophagic vesicles (green) in **Ir-1**-treated MDA-MB-231 cells. Nuclei were stained with DAPI (blue). Scale bar = 20 μm. (H) Representative confocal micrographs showing lipid peroxidation in **Ir-1**-treated MDA-MB-231 cells. The non-oxidized lipids (red) and oxidized lipids (green) were labeled with C11-BODIPY$^{581/591}$. Scale bar = 20 μm. Data are presented as mean ± SD (n = 3). *P < 0.05, as compared with the indicated group.

(Fer-1), showed that Fer-1 could significantly prevent **Ir-1**-induced cell death (Fig. 4C), suggesting that **Ir-1** induces ferroptosis as a mode of cell death as well. Thus, these results provide support for the suggestion that ferroptosis and autophagy play a primary role in regulating the cell death modes induced by **Ir-1**.

Subsequently, we conducted western blotting to assess the expression levels of cell death-associated marker proteins in **Ir-1**-treated MDA-MB-231 cells. The cleavage of pro-caspase-3, commonly employed as an indicator of apoptosis, was examined. Treatment with **Ir-1** did not considerably affect the expression level of pro-caspase-3, indicating that apoptosis was not associated with **Ir-1**-induced tumor cell death (Fig. 4D). As a common molecular marker of autophagy, the microtubule-associated protein light chain 3 (LC3) undergoes conversion from type I to type II during autophagy[69]. The results reveal an increase in the LC3-II level and LC3-II/LC3-I ratio after **Ir-1** treatment (Fig. 4E), suggesting that **Ir-1** can induce autophagy. Additionally, autophagy was assessed through confocal microscopy analysis using a green dye that selectively labels autophagic vesicles. The formation of autophagic vesicles in **Ir-1**-treated MDA-MB-231 cells increased, indicating the occurrence of autophagy (Fig. 4G). Solute carrier family 7 membrane 11 (SLC7A11) and glutathione peroxidase 4 (GPX4) are the key regulators of ferroptosis[70]. Inhibiting SLC7A11 and GPX4 activity can cause lipid peroxidation, ultimately leading to ferroptosis[71]. Western blotting revealed that the expression levels of SLC7A11 and GPX4 time-dependently decreased following **Ir-1** treatment (Fig. 4F), suggesting that **Ir-1** induced ferroptosis in MDA-MB-231 cells. As a key feature of ferroptosis, lipid peroxidation was assessed in MDA-MB-231 cells using a commercial dye C11-BODIPY$^{581/591}$[70]. Following incubation with **Ir-1**, MDA-MB-231 cells exhibited enhanced green fluorescence signals (Fig. 4H), indicating the induction of lipid peroxidation by **Ir-1**. As a prominent hallmark of lipid peroxidation, the production of malondialdehyde (MDA) in **Ir-1**-treated MDA-MB-231 cells were also significantly increased compared with that in the control (Supporting Information Fig. S5). These results provide support for the suggestion that **Ir-1** could induce cell death *via* autophagy and ferroptosis.

2.6. *Relation of ROS-mediated autophagy, ferroptosis, and ICD*

To confirm whether autophagy and ferroptosis were mediated by the ROS production induced by **Ir-1**, NAC was employed to block ROS generation. After pretreating MDA-MB-231 cells with NAC, the **Ir-1**-induced changes in the LC3-II level and LC3-II/LC3-I ratio were blocked (Fig. 5A). Simultaneously, the downregulated expression levels of SLC7A11 and GPX4 induced by **Ir-1** were reversed (Fig. 5B). Overall, these results indicate that autophagy and ferroptosis in MDA-MB-231 are dependent on the ROS production induced by **Ir-1**.

Recent studies have emphasized ferroptosis as a form of cell death that is dependent on autophagy[59,72,73]. To explore the potential relation between the autophagy and ferroptosis induced by **Ir-1**, we investigated the expression levels of related proteins in MDA-MB-231 cells in the presence of 3-MA and Fer-1,

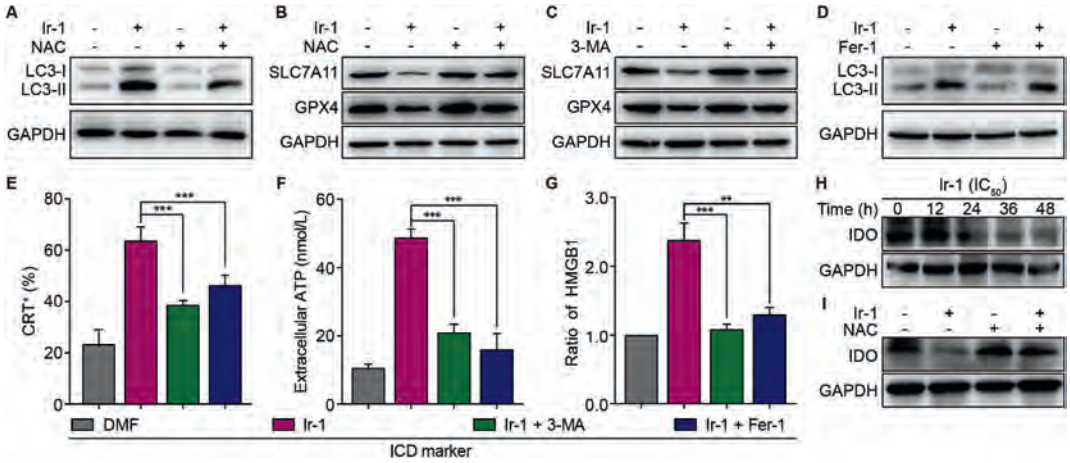

Figure 5 Relation of ROS-mediated autophagy, ferroptosis, ICD, and IDO inhibition. (A, B) Western blots of (A) autophagy or (B) ferroptosis markers after co-incubating MDA-MB-231 cells with NAC (10 mmol/L) and **Ir-1** (at IC_{50}) for 48 h. (C) Effects of inhibiting autophagy (by 2 mmol/L 3-MA) on the ferroptosis induced by **Ir-1** (at IC_{50}) in MDA-MB-231 cells. (D) Effects of inhibiting ferroptosis (by 2 μmol/L Fer-1) on the autophagy induced by **Ir-1** (at IC_{50}) in MDA-MB-231 cells. (E) Percentage of cells expressing surface-CRT after co-treating MDA-MB-231 cells with 3-MA (2 mmol/L) or Fer-1 (2 μmol/L) and **Ir-1** (6 μmol/L) for 12 h, as determined by flow cytometry. (F, G) Secretion of (F) ATP and (G) HMGB1 from MDA-MB-231 cells after co-treatment with **Ir-1** (at IC_{50}) and 3-MA (2 mmol/L) or Fer-1 (2 μmol/L) for 12 h. (H) Western blots of IDO after incubating MDA-MB-231 cells with **Ir-1**. (I) Western blots of IDO after co-incubating MDA-MB-231 cells with NAC (10 mmol/L) and **Ir-1** (at IC_{50}). Data are presented as mean ± SD ($n = 3$). $^{**}P < 0.01$, $^{***}P < 0.001$, as compared with the indicated group.

respectively. **Ir-1** could reduce the expression levels of SLC7A11 and GPX4 (Fig. 5C); however, this effect was significantly reversed after pretreatment with the autophagy inhibitor 3-MA. Conversely, the LC3-II level and LC3-II/LC3-I ratio did not significantly change after treatment with the ferroptosis inhibitor Fer-1 (Fig. 5D). Overall, **Ir-1** induces autophagy-dependent ferroptosis in MDA-MB-231 cells.

Recently, it has been reported that ferroptotic cells release ATP and HMGB1, two key DAMP signals of ICD[74,75]. Therefore, we investigated whether **Ir-1**-induced ICD is dependent on ferroptosis in MDA-MB-231 cells. Subsequently, we examined the changes in CRT exposure, ATP secretion, and HMGB1 release after pretreatment with ferroptosis inhibitor Fer-1. Immunofluorescence intensity of surface-CRT significantly decreased when cells were co-incubated with Fer-1 and **Ir-1** (Fig. 5E and S6). Moreover, ATP and HMGB1 secretion induced by **Ir-1** was significantly blocked by Fer-1 (Fig. 5F and G). These results suggest that inhibiting ferroptosis blocks the **Ir-1**-induced ICD activity. As anticipated, the autophagy inhibitor 3-MA also reversed the exposure or release of three ICD biomarkers induced by **Ir-1** (Fig. 5E−G and Supporting Information Fig. S6). Overall, **Ir-1** can induce autophagy-dependent ferroptosis and ferroptosis-dependent ICD activity.

2.7. *IDO inhibition induced by **Ir-1***

As a crucial negative feedback protein, IDO plays a pivotal role in shaping an immunosuppressive microenvironment conducive to tumor cell proliferation[76]. Notably, IDO overexpression in certain cancer cells causes the breakdown of tryptophan (TRP) and increase in TRP metabolites, causing the arrest of the cell cycle, demise of effector T cells, and proliferation of regulatory T cells[77-79]. A recent study indicated that IDO could inhibit ferroptosis[80]. IDO catalyzes the oxidation of TRP to kynurenine (KYN), which is subsequently converted to downstream metabolites that suppress ferroptosis. Thus, we investigated whether **Ir-1**-induced ferroptosis is related to the downregulation of IDO. The expression level of IDO in **Ir-1**-treated MDA-MB-231 cells was markedly downregulated (Fig. 5H). To explore the relation between ROS production and IDO expression downregulation, MDA-MB-231 cells were pretreated with NAC. The results revealed that the **Ir-1**-induced downregulation of IDO expression was blocked (Fig. 5I), demonstrating that **Ir-1**-induced ROS production could block IDO expression. These results provide support for the suggestion that **Ir-1** could inhibit ROS-mediated IDO expression.

2.8. *Antitumor vaccination in vivo*

MDA-MB-231 cells are a type of human-derived cancer cells; therefore, syngenetic TNBC 4T1 cells were selected for the subsequent *in vivo* experiments. As the gold standard of ICD evaluation, a vaccination model of 4T1 cells was established. Oxa was used as a positive control. In a first study, 2×10^6 4T1 cells were pretreated with different formulations (150 μmol/L Oxa, 20 μmol/L **Ir-1**, or only solvent) for 6 h. Subsequently, these cells were injected (s.c.) as a tumor vaccine into the left flanks of BALB/c mice ($n = 10$ per group). To observe the differences in tumor development between different groups during the rapid proliferation of 4T1 cells, after 7 days (Day 0), 1×10^4 untreated 4T1 cells were rechallenged in the right flanks of the mice. For 36 days, tumor formation in the right flanks was closely observed daily (Fig. 6A); mice that exhibited no tumor formation in their right flanks were documented as tumor-free mice. In the control group, tumors were observed in 20% of mice by Day 8 after rechallenge, and 100% of mice in this group developed tumors in the right flanks by Day 20. By contrast, the Oxa and **Ir-1** treatment groups exhibited a notable delay in tumor development after rechallenge (Fig. 6B). The first tumor in the Oxa group was detected on Day 10, whereas the first tumor in the **Ir-1** group appeared on Day 14. After 22 days, Oxa treatment produced a stable population of 30% tumor-free mice, whereas **Ir-1** treatment

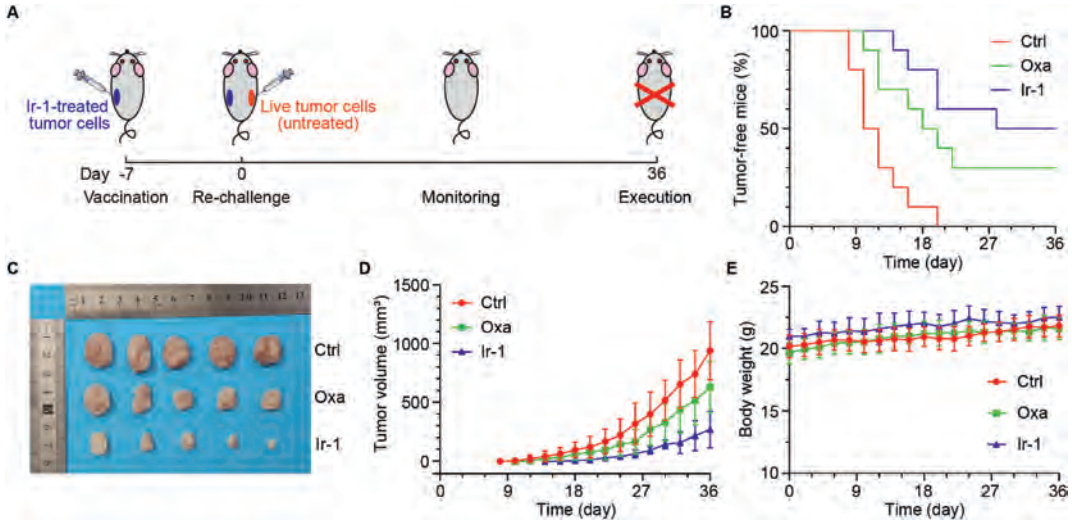

Figure 6 Anticancer vaccination. (A) ICD vaccine experiment of **Ir-1** using the TNBC 4T1 cell line. (B) Percentage of tumor-free mice following rechallenge with 4T1 cells. (C) Image of representative tumors dissected from the right flanks of mice 36 days after rechallenge. (D) Curves of tumor volume during treatments as determined *via* vaccination assays. (E) Curves of body weight during treatments as determined *via* vaccination assays. Data are presented as mean ± SD ($n = 10$).

exhibited a slower progression of tumorigenesis, ultimately achieving a stable population of 50% tumor-free mice after 28 days (Fig. 6C and D). In contrast to the control group, mice that were administered the **Ir-1**-treated vaccination cells exhibited significant inhibition of tumor growth. On the 36th day after inoculation, the average tumor volume in the **Ir-1** group was 274 mm^3, which was 2.31- and 3.45-fold smaller than those in the Oxa-treated (634 mm^3) and control (945 mm^3) groups, respectively. Furthermore, there were no significant differences observed in the body weights of mice among the different groups (Fig. 6E). These results demonstrate that **Ir-1** is a *bona fide* ICD inducer.

To confirm that differences in tumor growth were caused by *in vivo* immune responses, we used time-of-flight mass cytometry (CyTOF) to conduct high-dimensional characterization of tumors, spleens, lymph nodes, and peripheral blood samples from each group of mice in the vaccination assay. Live immune cells were first sorted using the $CD45^+$ marker antibody through a series of gating steps. Then, $CD8^+$ T cells, $CD4^+$ T cells, B cells, and macrophages/monocytes were identified based on classic markers (Supporting Information Table S2) from the live immune cell clusters. The two-dimensional *t*-stochastic neighbor embedding (*t*SNE) projections were constructed to compare the distinct landscapes of immune cells from the control and Oxa- and **Ir-1**-treated groups (Fig. 7A−D).

One of the key ICD responses *in vivo* is the activation of $CD8^+$ T cells within tumor sites[81]. $CD38^+$ is the marker protein of T cell activation[82], whereas the expression level of Ki67 serves as an indicator of the extent of cell proliferation[83]. We observed an increase in the proportions of $CD3^+CD8^+$, $CD3^+CD8^+CD38^+$, and $CD3^+CD8^+Ki67^+$ T cells in the four tested tissues after treatment with **Ir-1** or Oxa compared with those in the tissues treated with the control solvent (Fig. 7A−L). Specifically, in tumor tissues, the proportion of $CD3^+CD8^+$ T cell exhibited a significant increase, rising from 0.24% in the control group to 1.83% in the **Ir-1** treatment group and from 9.83% to 42.00%, and 31.32%−42.65% for $CD3^+CD8^+CD38^+$ and $CD3^+CD8^+Ki67^+$ T cells, respectively, which were all higher than the proportions of these cells in the Oxa-treated group (0.88%, 18.95%, and 37.41%, respectively; Fig. 7E and I). These results indicate that $CD3^+CD8^+$ T cells were fully activated following vaccination with **Ir-1**-treated cells. The proportions of cells expressing the cytokines tumor necrosis factor α (TNF-α), interferon γ (IFN-γ), and granzyme B (GZMB) reflect the killing capacity of $CD8^+$ T cells against tumor cells[84]. Higher percentages of cells expressing TNF-α (6.95%), IFN-γ (26.90%), and GZMB (26.30%) in $CD3^+CD8^+$ T cells were observed in the tumors treated with **Ir-1** compared with those in the control (3.92%, 14.53%, and 11.04%, respectively); these levels were also higher than those in the Oxa-treated group (5.65%, 17.88%, and 14.64%, respectively; Fig. 7I). $CD69^+$ is a marker used to identify tissue resident memory T cells (T_{RM}), which play a crucial role in providing long-term surveillance of tumor recurrence[85]. Compared with the control group, a notable increasing trend was observed in the proportion of $CD69^+$ cells in $CD3^+CD8^+$ T cells of tumors, spleens, and lymph nodes from the **Ir-1** group, which were also slightly higher than the proportions of cells from these tissues in the Oxa-treated group (Fig. 7I−K). These results further support that the ICD effect of cancer cells treated with **Ir-1** can activate the immune system to combat cancer, exhibiting a greater activity than that elicited by Oxa.

$CD4^+$ T cells are also crucial for regulating the immune responses of tumors[86]. The proportion of $CD3^+CD4^+$ T cells in tumors significantly increased from 1.31% in the control group to 5.97% in the **Ir-1**-treated group, and the proportion of Th cells ($CD4^+CD185^+$) also increased from 2.86% in the control group to 7.68% in the **Ir-1**-treated group; these proportions were slightly higher than those in the Oxa-treated group (4.71% and 6.85%, respectively; Fig. 7E and I). Treg cells ($CD3^+CD4^+Foxp3^+$ T cells) can inhibit the function of cytotoxic T cells by secreting immunosuppressive cytokines[87]. Compared with that in control group, a significant decrease of Treg cells in **Ir-1**-treated group was observed (Fig. 7I−L). The proportion of Treg cells in tumor tissues significantly decreased from 10.74% in the control group to 4.49% in the **Ir-1** treatment group (Fig. 7I). Overall,

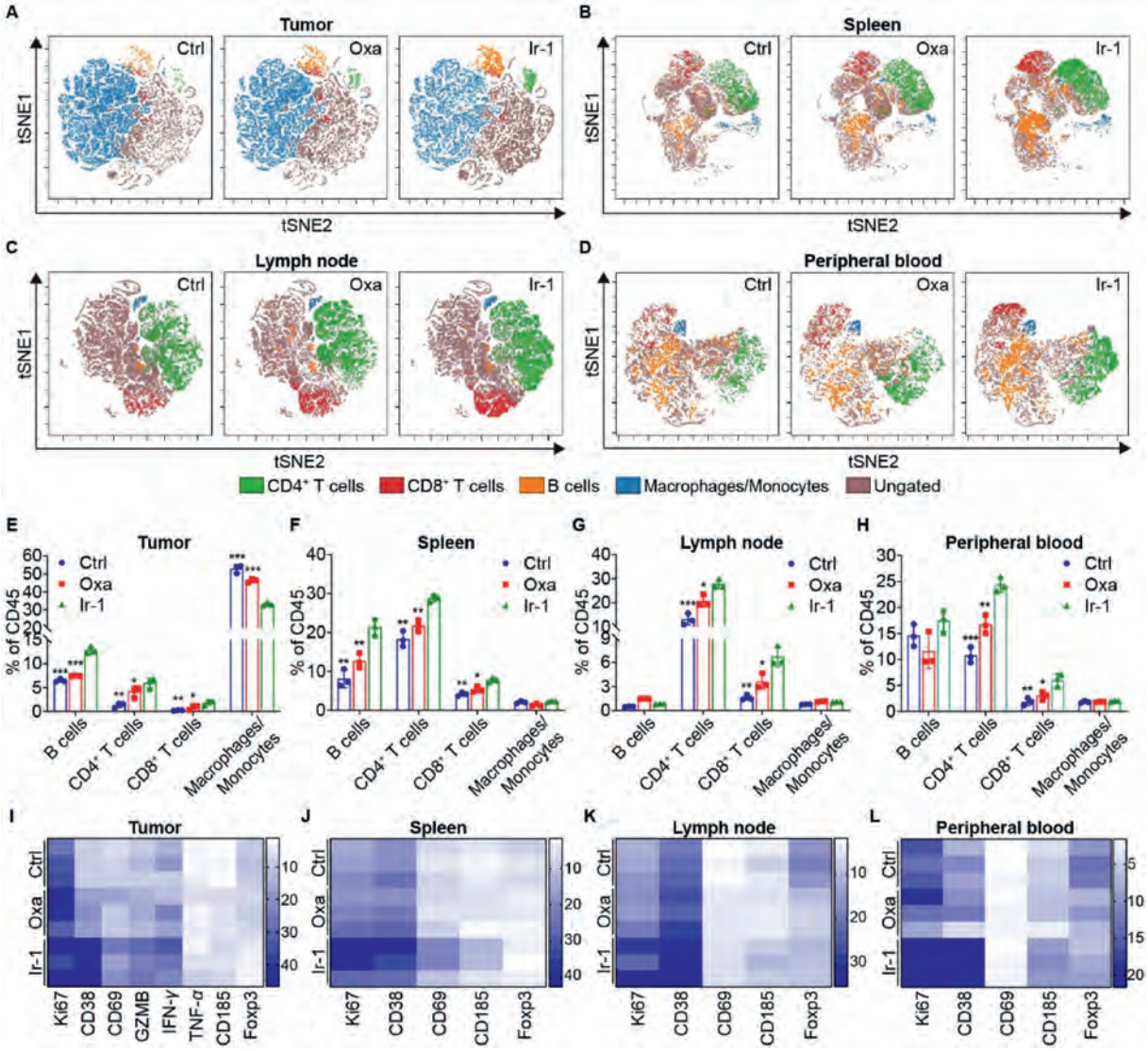

Figure 7 Analysis of immune cells using CyTOF. (A−D) tSNE maps showing distinct immune cell population in (A) tumors, (B) spleens, (C) lymph nodes, and (D) peripheral blood derived from each group of mice in the vaccination assay. (E−H) Quantitative data analysis of cell proportions in the corresponding mice tissues in (A−D). (I−L) Heatmaps showing the expression of distinct markers in (I) tumors, (J) spleens, (K) lymph nodes, and (L) peripheral blood. Data are presented as mean ± SD ($n = 3$). $^{*}P < 0.05$, $^{**}P < 0.01$, $^{***}P < 0.001$, as compared with the **Ir-1** group.

vaccination using cells treated with **Ir-1** can promote immune responses by downregulating Treg cells.

2.9. *In vivo therapeutic effect of **Ir-1***

After elucidating the mechanism by which **Ir-1** activates anticancer immunity, the anticancer efficacy of **Ir-1** was further validated *in vivo* using a murine model. First, the safety of **Ir-1** was assessed in BALB/c mice, with four mice per group. **Ir-1** was administered intravenously through the retro-orbital venous sinus once every 2 days at doses of 20, 30, and 40 mg/kg, respectively. While all mice survived, those administered with 40 mg/kg **Ir-1** exhibited a degree of loss in body weight compared with that in the control group (Supporting Information Fig. S7). Considering the changes in mice behavior and body weight, the 40 mg/kg dose was selected for the subsequent experiment.

We explored the therapeutic efficacy of **Ir-1** in a murine model of metastatic cancer *in vivo*. Studies have proven that ICD inducers have the potential to synergistically enhance the efficacy of PD-1/PD-L1 inhibitors[88-90]. Therefore, we wondered whether **Ir-1** therapy would synergize with PD-1 blockade to enhance antitumor effect. When the 4T1 tumor volume reached ~20 mm^3 (Day 0), the treatments, including anti-PD1 (10 mg/kg), Oxa (7 mg/kg), **Ir-1** (40 mg/kg), or anti-PD1 (10 mg/kg) and **Ir-1** (40 mg/kg) combination therapy, were injected (i.v.) into BALB/c mice bearing 4T1 tumors through the retro-orbital venous sinus once every 2 days. The selected doses and administration frequency were based on the condition of the mice and the safety profiles of the compounds. Under these conditions, while anti-PD1, Oxa, and **Ir-1** demonstrated significant tumor growth inhibition compared with the vehicle, the *in vivo* antitumor effect of **Ir-1** was superior to that of anti-PD1 or Oxa alone (Fig. 8A).

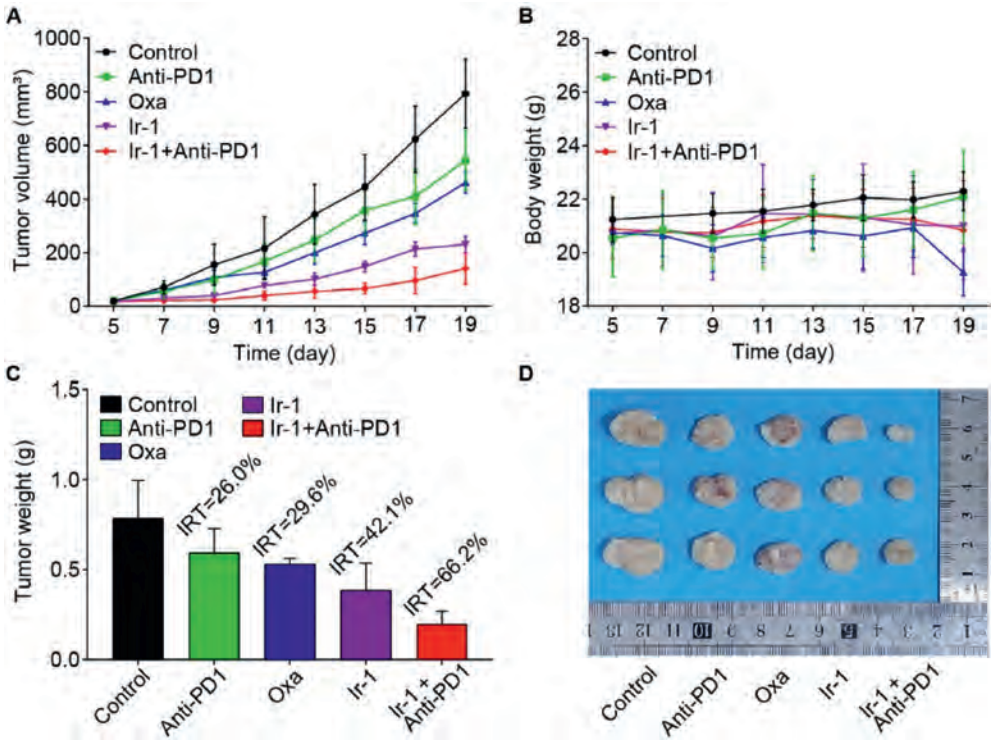

Figure 8 Anticancer therapy. (A) Tumor growth profiles of BALB/c mice bearing 4T1 tumors. (B) Effects of the indicated compounds or vehicle treatment on the body weight of BALB/c mice bearing 4T1 tumors. (C) Tumor weights and IRT values in BALB/c mice bearing 4T1 tumors after treatments on Day 19. (D) Image of representative tumors collected from the *in vivo* antitumor experiment. Data are presented as mean ± SD ($n = 6$).

Importantly, **Ir-1** and anti-PD1 combination therapy exerted the most pronounced antitumor effect (Fig. 8A). A notable disparity in body weight was evident in the **Ir-1**-treated group compared with that in the Oxa-treated group, with the Oxa-treated group exhibiting lower body weights than the **Ir-1**-treated group (Fig. 8B). These findings further emphasize the minimal side effects of **Ir-1** treatment. Upon completing the experiment, we collected and weighed the tumors, and determined the inhibition rate of tumor growth (IRT). **Ir-1** exhibited an IRT of 42.1%, surpassing those of Oxa (29.6%) and anti-PD1 (26.0%). Notably, **Ir-1** and anti-PD1 combination therapy demonstrated the highest IRT of 66.2% (Fig. 8C). These differences can also be observed from the image of tumors presented in Fig. 8D. Thus, **Ir-1** and anti-PD1 combination therapy exhibits significantly enhanced therapeutic effects *in vivo* while exhibiting reduced side effects compared with Oxa or anti-PD1 alone.

3. Conclusions

We designed and synthesized five cyclometalated Ir(III) complexes containing two isoquinoline ligands and an *N,N*-heterocyclic ligand. All Ir(III) complexes exhibited markedly high cytotoxicity (at 1.73−8.62 μmol/L), which was higher than that exhibited by cisplatin against the tested human cancer cell lines. Notably, **Ir-1** triggered an ICD effect in MDA-MB-231 cells by inducing ROS-mediated ER stress. The dominant mode of cell death contributing to the cytotoxicity induced by **Ir-1** was identified as autophagy-dependent ferroptosis mediated by ROS-induced ER stress. The ferroptosis inhibitor Fer-1 mitigated **Ir-1**-induced CRT exposure, ATP secretion, and HMGB1 release, indicating that **Ir-1** induces ferroptosis-dependent ICD in MDA-MB-231 cells. Moreover, the IDO blocking induced by **Ir-1** was mediated by ROS. *In vivo* results obtained from a tumor vaccination model of 4T1 cells further confirmed that **Ir-1** was a more efficient ICD inducer than Oxa and could significantly induce a change in the *in vivo* immune microenvironment. In the *in vivo* tumor growth experiment, **Ir-1** exhibited superior anticancer activity and lower toxicity compared with those exhibited by Oxa. Importantly, **Ir-1** and anti-PD1 combination therapy significantly enhanced *in vivo* therapeutic effects. Our study findings indicate that **Ir-1** is a promising chemoimmunotherapy candidate or model compound for developing anticancer drugs.

4. Experimental

4.1. Synthesis and characterization

The ligand L_a was firstly synthesized following a procedure described in our previous study[59]. Then, the general procedure for synthesizing compounds **Ir-1**−**Ir-5** is outlined as follows. The cyclometalated iridium(III) chloro-bridged dimer (c) was prepared according to a previously reported method[91]. $IrCl_3 \cdot 3H_2O$ (5 mmol) and ligand L_a (10 mmol) were added to a 6 mL mixture of 2-methoxylethanol (2-ME) and water (3:1, *v*/*v*). The mixture underwent reflux at 120 °C under a nitrogen atmosphere for 1 h. After filtering the solution, the filtrate was dried at 60 °C to yield compound (c). Then, as previously described[92], 0.14 mol of compound (c) and 0.3 mmol of N^N ligand (L_1, L_2, L_3 or L_4) were added to 5 mL of ethylene glycol, and the mixture was refluxed for 2 h at 120 °C under a nitrogen atmosphere. Once the solution

cooled to room temperature, an excess of KPF_6 solution was added, resulting in the formation of a precipitate. The solid precipitate was then filtered and left to dry at 60 °C overnight. The purification of the crude product was performed on a silica gel column (EA/MeOH, 9:1 *v*/*v*), yielding a bright-orange product (**Ir-1**, **Ir-2**, **Ir-3**, or **Ir-4**). In a separate reaction, 0.14 mol of compound (c) and 0.3 mmol of N^N ligand (L_5) were added to 10 mL of methanol. Subsequently, 0.6 mmol Na_2CO_3 was added, and the mixture was refluxed at 65 °C under a nitrogen atmosphere for 30 min. The as-obtained solution was concentrated, and the crude product was purified on a silica gel column (EA/MeOH, 9:1 *v*/*v*) to obtain the bright-orange product (**Ir-5**).

Data for Ir-1: Yield 60%. ^{1}H NMR (400 MHz, DMSO-d_6) δ 10.64 (s, 1H), 8.21 (s, 2H), 8.14 (d, J = 8.0 Hz, 2H), 8.04 (d, J = 6.4 Hz, 2H), 7.82 (ddd, J = 8.7, 7.2, 1.8 Hz, 2H), 7.64−7.53 (m, 4H), 7.41−7.30 (m, 4H), 7.09−6.94 (m, 2H), 6.78 (td, J = 7.7, 2.1 Hz, 4H), 6.35 (d, J = 3.2 Hz, 4H), 6.10 (dd, J = 7.6, 1.3 Hz, 2H). ^{13}C NMR (101 MHz, DMSO-d_6) δ 165.15, 152.47, 151.79, 151.26, 150.14, 149.11, 145.56, 140.85, 139.70, 135.96, 131.52, 129.54, 129.48, 122.78, 121.95, 120.78, 119.02, 115.47, 103.35, 102.84, 102.05. ESI-MS: *m*/*z* 860.19 $[M-PF_6]^+$.

Data for Ir-2: Yield 51%. ^{1}H NMR (400 MHz, DMSO-d_6) δ 8.89 (dd, J = 7.8, 1.9 Hz, 2H), 8.40 (s, 2H), 8.28−8.22 (m, 4H), 8.06−7.99 (m, 4H), 7.42 (s, 2H), 7.24 (d, J = 6.4 Hz, 2H), 7.14 (t, J = 6.7 Hz, 4H), 6.94 (td, J = 7.4, 1.2 Hz, 2H), 6.33 (d, J = 3.0 Hz, 4H), 6.26 (dd, J = 7.6, 1.3 Hz, 2H). ^{13}C NMR (101 MHz, DMSO-d_6) δ 165.21, 152.45, 151.81, 150.39, 150.27, 146.05, 145.74, 140.10, 138.78, 135.83, 131.68, 131.19, 129.88, 129.57, 128.39, 127.06, 122.72, 122.25, 121.32, 103.35, 102.89, 102.07. ESI-MS: *m*/*z* 869.17 $[M-PF_6]^+$.

Data for Ir-3: Yield 56%. ^{1}H NMR (600 MHz, DMSO-d_6) δ 8.69 (d, J = 8.0 Hz, 1H), 8.33 (t, J = 7.8 Hz, 1H), 8.28−8.16 (m, 4H), 7.77 (d, J = 8.3 Hz, 1H), 7.67 (dt, J = 13.3, 5.6 Hz, 2H), 7.51 (d, J = 6.3 Hz, 1H), 7.45 (d, J = 7.1 Hz, 2H), 7.42−7.32 (m, 4H), 7.16 (t, J = 7.7 Hz, 1H), 7.09 (t, J = 7.7 Hz, 1H), 6.96 (t, J = 7.9 Hz, 1H), 6.90 (q, J = 7.2 Hz, 2H), 6.31 (dd, J = 13.2, 5.1 Hz, 5H), 6.19 (d, J = 7.6 Hz, 1H), 5.91 (d, J = 8.4 Hz, 1H), 5.12 (s, 1H). ^{13}C NMR (151 MHz, DMSO-d_6) δ 165.73, 153.97, 153.68, 152.20, 152.13, 150.68, 150.64, 150.53, 150.28, 147.60, 146.44, 140.97, 140.75, 140.29, 140.22, 136.27, 136.09, 134.80, 132.82, 131.90, 130.29, 129.99, 129.58, 129.47, 129.00, 126.00, 124.78, 123.13, 122.96, 122.45, 122.30, 121.74, 121.67, 117.10, 114.22, 103.82, 103.79, 103.32, 103.27, 102.42, 102.37, 93.34. ESI-MS: *m*/*z* 884.19 $[M-PF_6]^+$.

Data for Ir-4: Yield 48%. ^{1}H NMR (600 MHz, DMSO-d_6) δ 8.92 (d, J = 8.2 Hz, 2H), 8.29−8.23 (m, 4H), 8.23−8.17 (m, 2H), 7.71 (t, J = 5.0 Hz, 2H), 7.66 (ddd, J = 6.9, 5.6, 1.2 Hz, 2H), 7.51−7.47 (m, 2H), 7.42 (d, J = 6.4 Hz, 2H), 7.35 (dd, J = 6.5, 3.4 Hz, 2H), 7.11−7.04 (m, 2H), 6.89 (t, J = 7.3 Hz, 2H), 6.33 (q, J = 4.4, 3.8 Hz, 4H), 6.17 (ddd, J = 7.5, 5.0, 2.1 Hz, 2H). ^{13}C NMR (151 MHz, DMSO-d_6) δ 165.13, 155.33, 153.08, 151.85, 150.30, 149.62, 145.52, 139.92, 139.61, 135.87, 131.48, 129.92, 129.59, 128.59, 125.07, 122.77, 122.14, 121.40, 103.41, 102.92, 102.07. ESI-MS: *m*/*z* 845.18 $[M-PF_6]^+$.

Data for Ir-5: Yield 53%. ^{1}H NMR (600 MHz, DMSO-d_6) δ 8.74 (d, J = 6.4 Hz, 1H), 8.27 (s, 1H), 8.21 (s, 1H), 8.13 (ddd, J = 8.0, 6.2, 1.3 Hz, 2H), 7.95 (td, J = 7.8, 1.7 Hz, 1H), 7.77 (d, J = 8.0 Hz, 1H), 7.64 (d, J = 6.4 Hz, 1H), 7.60−7.54 (m, 3H), 7.47 (d, J = 6.3 Hz, 1H), 7.42−7.39 (m, 1H), 7.28 (ddd, J = 7.5, 5.6, 1.5 Hz, 1H), 7.00 (ddd, J = 8.2, 7.1, 1.4 Hz, 1H), 6.94 (ddd, J = 8.2, 7.2, 1.4 Hz, 1H), 6.77 (td, J = 7.4, 1.2 Hz, 1H), 6.71 (td, J = 7.4, 1.2 Hz, 1H), 6.40−6.33 (m, 4H), 6.20 (dd, J = 7.7, 1.4 Hz, 1H), 6.13 (dd, J = 7.7, 1.3 Hz, 1H), 5.57 (tt, J = 8.0, 4.8 Hz, 1H), 4.98 (ddd, J = 12.6, 8.1, 5.1 Hz, 1H), 4.61 (ddd, J = 17.9, 7.8, 5.2 Hz, 1H), 4.34 (ddd, J = 18.0, 8.1, 4.9 Hz, 1H). ^{13}C NMR (151 MHz, DMSO-d_6) δ 166.35, 164.23, 156.65, 152.04, 151.29, 150.40, 148.67, 146.45, 146.11, 142.22, 140.48, 138.61, 136.36, 136.19, 132.95, 131.87, 129.93, 129.89, 129.35, 129.14, 125.54, 123.43, 123.36, 122.98, 121.66, 121.42, 121.09, 103.84, 103.71, 103.24, 102.69, 102.59, 49.62. ESI-MS: *m*/*z* 797.18 $[M-Cl]^+$.

4.2. *Immunofluorescent detection of cell surface CRT*

MDA-MB-231 cells were incubated with **Ir-1** at the specified concentration for 12 h in confocal dishes. After fixation and blocking, the cells were incubated with a primary anti-calreticulin antibody (Abcam, ab92516, Cambridge, UK) overnight at 4 °C. Then, the cells were washed and incubated with a secondary antibody (Abcam, ab150081, Cambridge, UK) for 2 h at room temperature. Upon removal of the antibody, the cells were stained with DAPI for 10 min. After washing again, the cells were stained with Wheat Germ Agglutinin (Invitrogen, W21404, Burlington, Canada) for 30 min at 37 °C. The immunofluorescence of CRT was visualized using confocal fluorescence microscopy.

4.3. *Extracellular HMGB1 detection assay*

HMGB1 release was assessed using an HMGB1 Detection Kit (Chondrex, 6010, Redmond, USA). MDA-MB-231 cells were seeded on a 10-cm dish at 1×10^6 cells/well overnight. The cells were then incubated with **Ir-1** for the specified duration. Following this treatment, the HMGB1 assay kit was utilized to determine the HMGB1 levels following the manufacturer's instructions. Luminescence was measured using a BioTek plate reader (Agilent, Cytation5, Winooski, USA).

4.4. *Extracellular ATP detection assay*

The secretion of ATP was quantified using an ATP Determination Kit (Invitrogen, A22066, Burlington, Canada). MDA-MB-231 cells were seeded on a 96-well plate at 1.5×10^4 cells/well overnight. Subsequently, cells were treated with **Ir-1** at the indicated concentration for the specified duration. Following this treatment, the ATP assay kit was used to assess the ATP levels following the manufacturer's instructions. Luminescence was measured using a BioTek plate reader (Agilent, Cytation5, Winooski, USA).

4.5. *Mouse vaccination assay*

Mice used in this study were purchased from Changsha's Animal Research Center (Hu Nan, China) and housed in the experimental animal facilities at the Guangxi Normal University under controlled temperature and humidity conditions with a 12-h light/12-h dark cycle. All mice had *ad libitum* access to commercial chow and water. All experimental procedures were executed according to the protocols approved by the Institutional Animal Care and Use Committee (IACUC) of Guangxi Normal University (Approval No: GXNU-202303-045). For the vaccination experiment, female BALB/c mice (5 weeks old, ~20 g) were used. A total of 2×10^6 4T1 cells in the logarithmic growth phase underwent various treatments for 6 h: normal medium for the control group (subjected to repeated freeze-thaw) and 20 μmol/L

Ir-1 or 150 μmol/L Oxa for each group ($n = 10$ per group). The treated 4T1 cells from each group were injected (s.c.) into the left flank of each mouse. After 7 days, the mice were rechallenged in the right flanks with untreated 4T1 cells (1×10^4 cells) and monitored daily for tumor formation on the right side. Mice without tumors in the right flanks were recorded as tumor-free. These observations continued until the end of the 36-day experiment, at which point the mice were euthanized. To uncover the underlying mechanism of the antitumor effect induced by **Ir-1**-treated 4T1 cell vaccination, a comprehensive analysis of immune cells was performed using CyTOF following standard methods. On Day 36, the mice from the control, Oxa, and **Ir-1** groups ($n = 10$) were euthanized. Tumors, spleens, and lymph nodes were dissected and grinded to obtain single-cell suspensions. Peripheral blood samples were collected *via* retro-orbital bleeding in heparin-coated tubes. Subsequently, cell suspensions were obtained *via* centrifugation at 1500 rpm for 5 min at 4 °C, followed by the removal of red blood cells at room temperature for 5 min and washing twice using 1 × PBS.

Acknowledgments

This study was supported by the National Natural Science Foundation of China (22177022, 22267005) and the Natural Science Foundation of Guangxi Province of China (AD22035193).

Author contributions

Yuan Lu: Investigation, Visualization, Writing − original draft, Formal analysis. Shan-Shan Wang: Investigation, Methodology, Visualization. Meng-Ya Li: Investigation, Methodology, Visualization. Rong Liu: Methodology, Visualization. Meng-Fan Zhu: Methodology, Visualization. Liang-Mei Yang: Methodology, Visualization. Feng-Yang Wang: Funding acquisition, Methodology. Ke-Bin Huang: Conceptualization, Project administration, Writing − review & editing. Hong Liang: Funding acquisition, Project administration, Supervision.

Conflicts of interest

The authors declare no conflicts of interest.

Appendix A. Supporting information

Supporting information to this article can be found online at https://doi.org/10.1016/j.apsb.2024.06.017.

References

1. Chhikara BS, Parang K. Global cancer statistics 2022: the trends projection analysis. *Chem Biol Lett* 2023;**10**:451.
2. Hon JD, Singh B, Sahin A, Du G, Wang J, Wang VY, et al. Breast cancer molecular subtypes: from TNBC to QNBC. *Am J Cancer Res* 2016;**6**:1864−72.
3. Hutchinson KE, Yost SE, Chang CW, Johnson RM, Carr AR, McAdam PR, et al. Comprehensive profiling of poor-risk paired primary and recurrent triple-negative breast cancers reveals immune phenotype shifts. *Clin Cancer Res* 2020;**26**:657−68.
4. Szekely B, Bossuyt V, Li X, Wali VB, Patwardhan GA, Frederick C, et al. Immunological differences between primary and metastatic breast cancer. *Ann Oncol* 2018;**29**:2232−9.
5. Schmid P, Adams S, Rugo HS, Schneeweiss A, Barrios CH, Iwata H, et al. Atezolizumab and nab-paclitaxel in advanced triple-negative breast cancer. *N Engl J Med* 2018;**379**:2108−21.
6. Adams S, Diamond JR, Hamilton E, Pohlmann PR, Tolaney SM, Chang CW, et al. Atezolizumab plus nab-paclitaxel in the treatment of metastatic triple-negative breast cancer with 2-year survival follow-up: a phase 1b clinical trial. *JAMA Oncol* 2019;**5**:334−42.
7. Galluzzi L, Buqué A, Kepp O, Zitvogel L, Kroemer G. Immunological effects of conventional chemotherapy and targeted anticancer agents. *Cancer Cell* 2015;**28**:690−714.
8. Rivera Vargas T, Apetoh L. Danger signals: chemotherapy enhancers?. *Immunol Rev* 2017;**280**:175−93.
9. Kroemer G, Galluzzi L, Kepp O, Zitvogel L. Immunogenic cell death in cancer therapy. *Annu Rev Immunol* 2013;**31**:51−72.
10. Krysko DV, Garg AD, Kaczmarek A, Krysko O, Agostinis P, Vandenabeele P. Immunogenic cell death and DAMPs in cancer therapy. *Nat Rev Cancer* 2012;**12**:860−75.
11. Garg AD, More S, Rufo N, Mece O, Sassano ML, Agostinis P, et al. Trial watch: immunogenic cell death induction by anticancer chemotherapeutics. *Oncoimmunology* 2017;**6**:1386829.
12. Wang Q, Ju X, Wang J, Fan Y, Ren M, Zhang H. Immunogenic cell death in anticancer chemotherapy and its impact on clinical studies. *Cancer Lett* 2018;**438**:17−23.
13. Flieswasser T, Van Loenhout J, Freire Boullosa L, Van den Eynde A, De Waele J, Van Audenaerde J, et al. Clinically relevant chemotherapeutics have the ability to induce immunogenic cell death in non-small cell lung cancer. *Cells* 2020;**9**:1474.
14. Huang KB, Wang FY, Feng HW, Luo H, Long Y, Zou T, et al. An aminophosphonate ester ligand-containing platinum(II) complex induces potent immunogenic cell death *in vitro* and elicits effective antitumour immune responses *in vivo*. *Chem Commun* 2019;**55**:13066−9.
15. Yamazaki T, Buqué A, Ames TD, Galluzzi L. PT-112 induces immunogenic cell death and synergizes with immune checkpoint blockers in mouse tumor models. *Oncoimmunology* 2020;**9**:1721810.
16. Sabbatini M, Zanellato I, Ravera M, Gabano E, Perin E, Rangone B, et al. Pt(IV) bifunctional prodrug containing 2-(2-propynyl)octanoato axial ligand: induction of immunogenic cell death on colon cancer. *J Med Chem* 2019;**62**:3395−406.
17. Sun Y, Yin E, Tan Y, Yang T, Song D, Jin S, et al. Immunogenicity and cytotoxicity of a platinum(IV) complex derived from capsaicin. *Dalton Trans* 2021;**50**:3516−22.
18. Novohradsky V, Markova L, Kostrhunova H, Kasparkova J, Hoeschele J, Brabec V. A [Pt(cis-1,3-diaminocycloalkane)Cl_2] analog exhibits hallmarks typical of immunogenic cell death inducers in model cancer cells. *J Inorg Biochem* 2022;**226**:111628.
19. Tham MJR, Babak MV, Ang WH. PlatinER: a highly potent anticancer platinum(II) complex that induces endoplasmic reticulum stress driven immunogenic cell death. *Angew Chem Int Ed* 2020;**59**:19070−8.
20. Novohradsky V, Pracharova J, Kasparkova J, Imberti C, Bridgewater HE, Sadler PJ, et al. Induction of immunogenic cell death in cancer cells by a photoactivated platinum(IV) prodrug. *Inorg Chem Front* 2020;**7**:4150−9.
21. Wong DY, Ong WW, Ang WH. Induction of immunogenic cell death by chemotherapeutic platinum complexes. *Angew Chem Int Ed Engl* 2015;**54**:6483−7.
22. Groer C, Zhang T, Lu R, Cai S, Mull D, Huang A, et al. Intratumoral cancer chemotherapy with a carrier-based immunogenic cell-death eliciting platinum (IV) agent. *Mol Pharm* 2020;**17**:4334−45.
23. Deng Z, Wang N, Liu Y, Xu Z, Wang Z, Lau TC, et al. A photocaged, water-oxidizing, and nucleolus-targeted Pt(IV) complex with a distinct anticancer mechanism. *J Am Chem Soc* 2020;**142**:7803−12.
24. Wong DYQ, Yeo CHF, Ang WH. Immuno-chemotherapeutic platinum(IV) prodrugs of cisplatin as multimodal anticancer agents. *Angew Chem Int Ed* 2014;**53**:6752−6.
25. Bian M, Fan R, Yang Z, Chen Y, Xu Z, Lu Y, et al. Pt(II)-NHC complex induces ROS-ERS-related DAMP balance to harness

immunogenic cell death in hepatocellular carcinoma. *J Med Chem* 2022;**65**:1848−66.
26. Su X, Liu B, Wang WJ, Peng K, Liang BB, Zheng Y, et al. Disruption of zinc homeostasis by a novel platinum(IV)-terthiophene complex for antitumor immunity. *Angew Chem Int Ed* 2023;**62**:e202216917.
27. Wernitznig D, Kiakos K, Del Favero G, Harrer N, Machat H, Osswald A, et al. First-in-class ruthenium anticancer drug (KP1339/IT-139) induces an immunogenic cell death signature in colorectal spheroids *in vitro*. *Metallomics* 2019;**11**:1044−8.
28. Konda P, Lifshits LM, Roque Iii JA, Cole HD, Cameron CG, McFarland SA, et al. Discovery of immunogenic cell death-inducing ruthenium-based photosensitizers for anticancer photodynamic therapy. *Oncoimmunology* 2021;**10**:1863626.
29. Wernitznig D, Meier-Menches SM, Cseh K, Theiner S, Wenisch D, Schweikert A, et al. Plecstatin-1 induces an immunogenic cell death signature in colorectal tumour spheroids. *Metallomics* 2020;**12**: 2121−33.
30. Xu Z, Xu M, Wu X, Guo S, Tian Z, Zhu D, et al. A half-sandwich ruthenium(II) (N^N) complex: inducing immunogenic melanoma cell death *in vitro* and *in vivo*. *ChemMedChem* 2023;**18**:e202300131.
31. Wang L, Guan R, Xie L, Liao X, Xiong K, Rees TW, et al. An ER-targeting iridium(III) complex that induces immunogenic cell death in non-small-cell lung cancer. *Angew Chem Int Ed Engl* 2021;**60**: 4657−65.
32. Ji S, Yang X, Chen X, Li A, Yan D, Xu H, et al. Structure-tuned membrane active Ir-complexed oligoarginine overcomes cancer cell drug resistance and triggers immune responses in mice. *Chem Sci* 2020;**11**:9126−33.
33. Vigueras G, Markova L, Novohradsky V, Marco A, Cutillas N, Kostrhunova H, et al. A photoactivated Ir(III) complex targets cancer stem cells and induces secretion of damage-associated molecular patterns in melanoma cells characteristic of immunogenic cell death. *Inorg Chem Front* 2021;**8**:4696−711.
34. Ling YY, Wang WJ, Hao L, Wu XW, Liang JH, Zhang H, et al. Self-amplifying iridium(III) photosensitizer for ferroptosis-mediated immunotherapy against transferrin receptor-overexpressing cancer. *Small* 2022;**18**:2203659.
35. Wang WJ, Ling YY, Zhong YM, Li ZY, Tan CP, Mao ZW. Ferroptosis-enhanced cancer immunity by a ferrocene-appended iridium(III) diphosphine complex. *Angew Chem Int Ed* 2022;**61**:e202115247.
36. Wang L, Karges J, Wei F, Xie L, Chen Z, Gasser G, et al. A mitochondria-localized iridium(III) photosensitizer for two-photon photodynamic immunotherapy against melanoma. *Chem Sci* 2023; **14**:1461−71.
37. Ling YY, Kong YJ, Hao L, Pan ZY, Mao ZW, Tan CP. Photodegradation of carbonic anhydrase by iridium complexes for induction of immunogenic cell death under hypoxia. *Inorg Chem Front* 2023;**10**:3284−92.
38. Xiong X, Huang KB, Wang Y, Cao B, Luo Y, Chen H, et al. Target profiling of an iridium(III)-based immunogenic cell death inducer unveils the engagement of unfolded protein response regulator BiP. *J Am Chem Soc* 2022;**144**:10407−16.
39. Rong Y, Fan Z, Yu Z, Wei L, Shen H, Huang H, et al. An endoplasmic reticulum-targeting iridium(III) complex induces immunogenic cell death in melanoma cells and enhances anti-PD-1 immunotherapy by remodeling tumor microenvironment. *Inorg Chem Front* 2023;**10**: 5278−91.
40. Kaur P, Johnson A, Northcote-Smith J, Lu C, Suntharalingam K. Immunogenic cell death of breast cancer stem cells induced by an endoplasmic reticulum-targeting copper(II) complex. *Chembiochem* 2020;**21**:3618−24.
41. Le HV, Babak MV, Ehsan MA, Altaf M, Reichert L, Gushchin AL, et al. Highly cytotoxic gold(I)-phosphane dithiocarbamate complexes trigger an ER stress-dependent immune response in ovarian cancer cells. *Dalton Trans* 2020;**49**:7355−63.
42. Sen S, Hufnagel S, Maier EY, Aguilar I, Selvakumar J, DeVore JE, et al. Rationally designed redox-active Au(I) N-heterocyclic carbene: an immunogenic cell death inducer. *J Am Chem Soc* 2020;**142**: 20536−41.
43. Mule RD, Kumar A, Sancheti SP, Senthilkumar B, Kumar H, Patil NT. BQ-AurIPr: a redox-active anticancer Au(I) complex that induces immunogenic cell death. *Chem Sci* 2022;**13**:10779−85.
44. Yang Z, Bian M, Lv L, Chang X, Wen Z, Li F, et al. Tumor-targeting NHC−Au(I) complex induces immunogenic cell death in hepatocellular carcinoma. *J Med Chem* 2023;**66**:3934−52.
45. Xu Z, Lu Q, Shan M, Jiang G, Liu Y, Yang Z, et al. NSAID−Au(I) complexes induce ROS-driven DAMPs and interpose inflammation to stimulate the immune response against ovarian cancer. *J Med Chem* 2023;**66**:7813−33.
46. Lu Y, Sheng X, Liu C, Liang Z, Wang X, Liu L, et al. SERD-NHC-Au(I) complexes for dual targeting ER and TrxR to induce ICD in breast cancer. *Pharmacol Res* 2023;**190**:106731.
47. Li F, Wen Z, Wu C, Yang Z, Wang Z, Diao W, et al. Simultaneous activation of immunogenic cell death and cGAS-STING pathway by liver- and mitochondria-targeted gold(I) complexes for chemo-immunotherapy of hepatocellular carcinoma. *J Med Chem* 2024;**67**: 1982−2003.
48. Wang FX, Liu JW, Hong XQ, Tan CP, Zhang L, Chen WH, et al. Anion-responsive manganese porphyrin facilitates chloride transport and induces immunogenic cell death. *CCS Chem* 2022;**4**:2409−19.
49. Su X, Wang WJ, Cao Q, Zhang H, Liu B, Ling Y, et al. A carbonic anhydrase IX (CAIX)-anchored rhenium(I) photosensitizer evokes pyroptosis for enhanced anti-tumor immunity. *Angew Chem Int Ed* 2022;**61**:e202115800.
50. Kepp O, Marabelle A, Zitvogel L, Kroemer G. Oncolysis without viruses—inducing systemic anticancer immune responses with local therapies. *Nat Rev Clin Oncol* 2020;**17**:49−64.
51. Gasser G, Metzler-Nolte N. The potential of organometallic complexes in medicinal chemistry. *Curr Opin Chem Biol* 2012;**16**:84−91.
52. Cutillas N, Yellol GS, de Haro C, Vicente C, Rodríguez V, Ruiz J. Anticancer cyclometalated complexes of platinum group metals and gold. *Coord Chem Rev* 2013;**257**:2784−97.
53. Omae I. Applications of five-membered ring products of cyclometalation reactions as anticancer agents. *Coord Chem Rev* 2014;**280**: 84−95.
54. Shahsavari HR, Hu J, Chamyani S, Sakamaki Y, Aghakhanpour RB, Salmon C, et al. Fluorinated cycloplatinated(II) complexes bearing bisphosphine ligands as potent anticancer agents. *Organometallics* 2021;**40**:72−82.
55. Chen ZF, Liu YC, Huang KB, Liang H. Alkaloid-metal based anticancer agents. *Curr Top Med Chem* 2013;**13**:2104−15.
56. Ma DL, Wu C, Cheng SS, Lee FW, Han QB, Leung CH. Development of natural product-conjugated metal complexes as cancer therapies. *Int J Mol Sci* 2019;**20**:341.
57. Huang KB, Wang FY, Tang XM, Feng HW, Chen ZF, Liu YC, et al. Organometallic gold(III) complexes similar to tetrahydroisoquinoline induce ER-stress-mediated apoptosis and pro-death autophagy in A549 cancer cells. *J Med Chem* 2018;**61**:3478−90.
58. Huang KB, Mo HY, Chen ZF, Wei JH, Liu YC, Liang H. Isoquinoline derivatives Zn(II)/Ni(II) complexes: crystal structures, cytotoxicity, and their action mechanism. *Eur J Med Chem* 2015;**100**:68−76.
59. Wang FY, Yang LM, Wang SS, Lu H, Wang XS, Lu Y, et al. Cycloplatinated (II) complex based on isoquinoline alkaloid elicits ferritinophagy-dependent ferroptosis in triple-negative breast cancer cells. *J Med Chem* 2024;**67**:6738−48.
60. Sen S, Won M, Levine MS, Noh Y, Sedgwick AC, Kim JS, et al. Metal-based anticancer agents as immunogenic cell death inducers: the past, present, and future. *Chem Soc Rev* 2022;**51**:1212−33.
61. Galluzzi L, Buqué A, Kepp O, Zitvogel L, Kroemer G. Immunogenic cell death in cancer and infectious disease. *Nat Rev Immunol* 2017;**17**: 97−111.
62. Wadgaonkar P, Chen F. Connections between endoplasmic reticulum stress-associated unfolded protein response, mitochondria, and autophagy in arsenic-induced carcinogenesis. *Semin Cancer Biol* 2021;**76**: 258−66.
63. Ramos R, Gilles JF, Morichon R, Przybylski C, Caron B, Botuha C, et al. Cytotoxic BODIPY-appended half-sandwich iridium(III)

complex forms protein adducts and induces ER stress. *J Med Chem* 2021;**64**:16675−86.
64. Yuan B, Liu J, Guan R, Jin C, Ji L, Chao H. Endoplasmic reticulum targeted cyclometalated iridium(III) complexes as efficient photodynamic therapy photosensitizers. *Dalton Trans* 2019;**48**:6408−15.
65. Zhou L, Wei F, Xiang J, Li H, Li C, Zhang P, et al. Enhancing the ROS generation ability of a rhodamine-decorated iridium(III) complex by ligand regulation for endoplasmic reticulum-targeted photodynamic therapy. *Chem Sci* 2020;**11**:12212−20.
66. Cathcart R, Schwiers E, Ames BN. Detection of picomole levels of hydroperoxides using a fluorescent dichlorofluorescein assay. *Anal Biochem* 1983;**134**:111−6.
67. Su LJ, Zhang JH, Gomez H, Murugan R, Hong X, Xu D, et al. Reactive oxygen species-induced lipid peroxidation in apoptosis, autophagy, and ferroptosis. *Oxid Med Cel Longev* 2019;**2019**: 5080843.
68. Seglen PO, Gordon PB. 3-Methyladenine: specific inhibitor of autophagic/lysosomal protein degradation in isolated rat hepatocytes. *Proc Natl Acad Sci U S A* 1982;**79**:1889−92.
69. Kabeya Y, Mizushima N, Ueno T, Yamamoto A, Kirisako T, Noda T, et al. LC3, a mammalian homologue of yeast Apg8p, is localized in autophagosome membranes after processing. *EMBO J* 2000;**19**: 5720−8.
70. Chen X, Comish PB, Tang D, Kang R. Characteristics and biomarkers of ferroptosis. *Front Cel Dev Biol* 2021;**9**:637162.
71. Lei P, Bai T, Sun Y. Mechanisms of ferroptosis and relations with regulated cell death: a review. *Front Physiol* 2019;**10**:139.
72. Li J, Liu J, Xu Y, Wu R, Chen X, Song X, et al. Tumor heterogeneity in autophagy-dependent ferroptosis. *Autophagy* 2021;**17**:3361−74.
73. Zhou B, Liu J, Kang R, Klionsky DJ, Kroemer G, Tang D. Ferroptosis is a type of autophagy-dependent cell death. *Semin Cancer Biol* 2020; **66**:89−100.
74. Wen Q, Liu J, Kang R, Zhou B, Tang D. The release and activity of HMGB1 in ferroptosis. *Biochem Biophys Res Commun* 2019;**510**: 278−83.
75. Efimova I, Catanzaro E, Van der Meeren L, Turubanova VD, Hammad H, Mishchenko TA, et al. Vaccination with early ferroptotic cancer cells induces efficient antitumor immunity. *J Immunother Cancer* 2020;**8**:e001369.
76. Meireson A, Devos M, Brochez L. IDO expression in cancer: different compartment, different functionality? *Front Immunol* 2020;**11**:531491.
77. Platten M, Nollen EAA, Röhrig UF, Fallarino F, Opitz CA. Tryptophan metabolism as a common therapeutic target in cancer, neurodegeneration and beyond. *Nat Rev Drug Discov* 2019;**18**:379−401.
78. Labadie BW, Bao R, Luke JJ. Reimagining IDO pathway inhibition in cancer immunotherapy *via* downstream focus on the tryptophan-kynurenine-aryl hydrocarbon axis. *Clin Cancer Res* 2019;**25**: 1462−71.
79. Platten M, Wick W, Van den Eynde BJ. Tryptophan catabolism in cancer: beyond IDO and tryptophan depletion. *Cancer Res* 2012;**72**: 5435−40.
80. Fiore A, Zeitler L, Russier M, Groß A, Hiller M-K, Parker JL, et al. Kynurenine importation by SLC7A11 propagates anti-ferroptotic signaling. *Mol Cel* 2022;**82**:920−32.
81. Qiu X, Qu Y, Guo B, Zheng H, Meng F, Zhong Z. Micellar paclitaxel boosts ICD and chemo-immunotherapy of metastatic triple negative breast cancer. *J Controlled Release* 2022;**341**:498−510.
82. Wu P, Zhao L, Chen Y, Xin Z, Lin M, Hao Z, et al. CD38 identifies pre-activated $CD8^+$ T cells which can be reinvigorated by anti-PD-1 blockade in human lung cancer. *Cancer Immunol Immunother* 2021; **70**:3603−16.
83. Sun X, Kaufman PD. Ki-67: more than a proliferation marker. *Chromosoma* 2018;**127**:175−86.
84. Farhood B, Najafi M, Mortezaee K. $CD8^+$ cytotoxic T lymphocytes in cancer immunotherapy: a review. *J Cel Physiol* 2019;**234**:8509−21.
85. Park SL, Gebhardt T, Mackay LK. Tissue-resident memory T cells in cancer immunosurveillance. *Trends Immunol* 2019;**40**:735−47.
86. Smith CM, Wilson NS, Waithman J, Villadangos JA, Carbone FR, Heath WR, et al. Cognate $CD4^+$ T cell licensing of dendritic cells in $CD8^+$ T cell immunity. *Nat Immunol* 2004;**5**:1143−8.
87. von Boehmer H, Daniel C. Therapeutic opportunities for manipulating TReg cells in autoimmunity and cancer. *Nat Rev Drug Discov* 2013; **12**:51−63.
88. Limagne E, Thibaudin M, Nuttin L, Spill A, Derangere V, Fumet JD, et al. Trifluridine/tipiracil plus oxaliplatin improves PD-1 blockade in colorectal cancer by inducing immunogenic cell death and depleting macrophages. *Cancer Immunol Res* 2019;**7**:1958−69.
89. Yu J, He X, Wang Z, Wang Y, Liu S, Li X, et al. Combining PD-L1 inhibitors with immunogenic cell death triggered by chemo-photothermal therapy *via* a thermosensitive liposome system to stimulate tumor-specific immunological response. *Nanoscale* 2021;**13**: 12966−78.
90. Kepp O, Zitvogel L, Kroemer G. Clinical evidence that immunogenic cell death sensitizes to PD-1/PD-L1 blockade. *Oncoimmunology* 2019; **8**:1637188.
91. Li G, Chen Y, Wu J, Ji L, Chao H. Thiol-specific phosphorescent imaging in living cells with an azobis(2,2′-bipyridine)-bridged dinuclear iridium(III) complex. *Chem Commun* 2013;**49**:2040−2.
92. Li GN, Gao CW, Xie H, Chen HH, Liu D, Sun W, et al. New luminescent cyclometalated iridium(III) complexes containing fluorinated phenylisoquinoline-based ligands: synthesis, structures, photophysical properties and DFT calculations. *Chin Chem Lett* 2016;**27**:428−32.